

# Ba<sub>2</sub>Si<sub>3</sub>P<sub>6</sub>: 1D Nonlinear Optical Material with Thermal Barrier Chains

Justin Mark,<sup>a,b</sup> Jian Wang,<sup>a,b</sup> Kui Wu,<sup>c</sup> Jeane Gladys Lo,<sup>d</sup> Shannon Lee,<sup>a,b</sup> Kirill Kovnir<sup>a,b,\*</sup>

<sup>a</sup> Department of Chemistry, Iowa State University, Ames, Iowa 50011, USA

<sup>b</sup> Ames Laboratory, U.S. Department of Energy, Ames, Iowa 50011, USA

<sup>c</sup> College of Chemistry and Environmental Science, Hebei University, Key Laboratory of Analytical Science and Technology of Hebei Province, Baoding 0710002, China

<sup>d</sup> Department of Chemistry, University of California, Davis, Davis CA 95616, USA

\* Corresponding author, e-mail: [kovnir@iastate.edu](mailto:kovnir@iastate.edu)

**ABSTRACT:** A novel barium silicon phosphide was synthesized and characterized. Ba<sub>2</sub>Si<sub>3</sub>P<sub>6</sub> crystallizes in the non-centrosymmetric space group *Pna*2<sub>1</sub> (No. 33) and exhibits a unique bonding connectivity in the Si-P polyanion not found in other compounds. The crystal structure is composed of SiP<sub>4</sub> tetrahedra connected into one-dimensional double-tetrahedra chains through corner sharing, edge sharing, and covalent P-P bonds. Chains are surrounded by Ba cations to achieve an electron balance. The novel compound exhibits semiconducting properties with a calculated bandgap of 1.6 eV and experimental optical bandgap of 1.88 eV. The complex pseudo one-dimensional structure manifests itself in the transport and optical properties of Ba<sub>2</sub>Si<sub>3</sub>P<sub>6</sub>, demonstrating ultra-low thermal conductivity (0.56 W m<sup>-1</sup> K<sup>-1</sup> at 300 K), promising second harmonic generation signal (0.9×AgGaS<sub>2</sub>), as well as high laser damage threshold (1.6×AgGaS<sub>2</sub>, 48.5 MW/cm<sup>2</sup>) when compared to the benchmark material AgGaS<sub>2</sub>. Differential scanning calorimetry reveals that Ba<sub>2</sub>Si<sub>3</sub>P<sub>6</sub> melts congruently at 1373 K, suggesting that large single crystal growth may be possible.

## Introduction

Ternary tetrel-pnictides exhibit a diverse structural chemistry leading to fascinating properties. For example, an incorporation of Li or Na into the interlayer space of binary tin phosphides and arsenides resulted in unexpected thermal and superconducting properties.<sup>1-3</sup> NaSn<sub>2</sub>As<sub>2</sub> and Na<sub>1-x</sub>Sn<sub>2</sub>P<sub>2</sub> were shown to be superconductors at 1.3 K and 2.0 K respectively, revealing that Sn<sub>2</sub>Pn<sub>2</sub> layers may be a basic layered building block exhibiting superconducting properties.<sup>2,3</sup> In ternary phases, tin atoms are octahedrally coordinated similar to the tin coordination in binary pnictides Sn<sub>4</sub>P<sub>3</sub>, Sn<sub>4</sub>As<sub>3</sub>, and Sn<sub>3</sub>P<sub>4</sub>.<sup>4</sup> Pnictides of lighter tetrrels have different structural chemistry due to the tetra-coordinated nature of Si and Ge. Binary tetrel-pnictides, *Tt-Pn* (*Tt* = Si, Ge; *Pn* = P, As) phases are composed of layers with either *TtPn* or *TtPn*<sub>2</sub> stoichiometry.<sup>5-10</sup> In both cases, the layers are terminated by the pnictogen element which is covalently bonded to three neighbors and has an electron lone pair pointed towards the electron lone pairs on pnictogen atoms terminating neighboring layers. The repulsion of the electron lone-pairs is responsible for the two-dimensional crystal structure with weak van der Waals type interactions between the layers. The binary tetrel-pnictides have been considered for numerous potential applications in batteries, thermoelectrics, photovoltaics, field-effect transistors, and infrared photodetectors.<sup>4,11-20</sup>

Ternary tetrel-pnictides where the *Tt-Pn* polyanion is modified through interactions with electropositive cations exhibit diverse structural chemistry which further expand the range of potential applications. The versatility in bonding in the polyanion results in crystal structures with different dimensionality ranging from 0D (Li<sub>8</sub>SiP<sub>4</sub>, AE<sub>4</sub>TtP<sub>4</sub>; AE = Ca, Sr, Ba; *Tt* = Si, Ge), 1D (K<sub>2</sub>SiP<sub>2</sub>, Ba<sub>4</sub>Si<sub>3</sub>P<sub>8</sub>, Ca<sub>3</sub>Si<sub>2</sub>P<sub>4</sub>), 2D (LiGe<sub>3</sub>As<sub>3</sub>, Li<sub>3</sub>Si<sub>7</sub>As<sub>8</sub>, Ca<sub>2</sub>Si<sub>2</sub>P<sub>4</sub>, NaGe<sub>6</sub>As<sub>6</sub>, Ba<sub>3</sub>Si<sub>4</sub>P<sub>6</sub>), and 3D (Li<sub>2</sub>SiP<sub>2</sub>, MgSiAs<sub>2</sub>, Mg<sub>3</sub>Si<sub>6</sub>As<sub>8</sub>, AE<sub>2</sub>SiP<sub>4</sub>; AE = Sr, Eu, Ba).<sup>13,21-28</sup>

One potential application of ternary tetrel-pnictides is infrared non-linear optical materials, where the non-centrosymmetric crystal structure is a prerequisite coupled with a suitable bandgap, high laser damage threshold, good chemical and thermal stability, and moderate mechanical properties, such as hardness.<sup>29-35</sup> This field is dominated by late- and post-transition metal chalcogenide materials.<sup>32-39</sup> Besides scarcity and toxicity of metals such as Ge, Cd, and Hg, the metal-chalcogen bonds are polar and have only moderate strength thus limiting the materials applications. The global aim of our work is to find materials with stronger covalent bonding between earth-abundant elements, such as Si and P. Synthesizing non-centrosymmetric phases is no straightforward task, however analysis of the reported compounds in AE-*Tt-Pn* systems (AE = alkaline-earth metal) reveals that a large fraction of ternary tetrel-pnictides crystallize in non-centrosymmetric structures.<sup>21,23,24,27</sup> We

hypothesized that the repulsion of the electron-lone pairs located on pnictogen atoms is responsible for such unusually high abundance of non-centrosymmetric compounds. Typically, *AE-Tt-Pn* compounds are electron-balanced with bandgaps suitable for infrared applications. We verified our hypothesis by studying the ternary Mg-Si-As system where no phases were experimentally reported and found two new non-centrosymmetric compounds,  $\text{Mg}_3\text{Si}_6\text{As}_8$  and  $\text{MgSiAs}_2$ .<sup>27</sup> The latter is a promising non-linear optical material with a second harmonic generation signal and laser damage threshold comparable to state-of-the-art material,  $\text{AgGaS}_2$ . Using less toxic and more abundant P instead of As should strengthen the covalent interactions in the silicon-pnictide polyanion leading to higher stability, corresponding to a higher laser damage threshold. Our search has resulted in the novel phase  $\text{Ba}_2\text{Si}_3\text{P}_6$  which crystallizes in the non-centrosymmetric *Pna*2<sub>1</sub> space group (No. 33) with a suitable bandgap for infrared second harmonic generation. In this work we report on the synthesis, crystal and electronic structure, transport, and optical properties of  $\text{Ba}_2\text{Si}_3\text{P}_6$ .

### Experimental

All handling of materials was done in an argon filled glove box with  $\text{O}_2$  levels < 0.5 ppm. The starting materials were metallic Ba (Sigma Aldrich, 99.9%), Si powder (Alfa Aesar, 99.99%), and red P powder (Alfa Aesar, 98.9%). A single crystal of  $\text{Ba}_2\text{Si}_3\text{P}_6$  was first obtained from a sample of nominal composition “ $\text{BaSi}_6\text{P}_8$ ” which was heated to 1223 K over 17 hours and annealed for 48 hours. Near single phase samples of  $\text{Ba}_2\text{Si}_3\text{P}_6$  were prepared by loading a stoichiometric ratio of the elements in carbonized silica ampoules (Figures S1 and S2). Ampoules were evacuated, and flame sealed. The ampoules were then heated in a muffle furnace to 1273 K over 10 hours and annealed at this temperature for 72 hours. The resulting product was a metallic gray chunk which turned red upon grinding into powder.  $\text{Ba}_2\text{Si}_3\text{P}_6$  is highly-moisture sensitive and moderately air-sensitive. Degradation is detected by powder X-ray diffraction after 30 minutes of humid air exposure, but only slight background increase was observed for sample stored 3 days in a desiccator (Figure S3). Further experimental details regarding characterization methods can be found in the Supporting Information.

### Results/Discussion

$\text{Ba}_2\text{Si}_3\text{P}_6$  crystallizes in the non-centrosymmetric orthorhombic space group *Pna*2<sub>1</sub> (No. 33) with cell parameters  $a = 9.6272(4)$  Å,  $b = 9.1437(4)$  Å, and  $c = 11.9261(6)$  Å. Details regarding data collection, refinement parameters, and crystal structure for  $\text{Ba}_2\text{Si}_3\text{P}_6$  can be found in Tables S1-S4. The crystal structure is composed of double-tetrahedra Si-P chains running along the [100] direction surrounded by Ba cations (Figure 1). Each chain is built from  $\text{SiP}_4$  tetrahedra which are interconnected through corner sharing, edge sharing, and covalent P-P bonds (Figures 1 and 2D).  $\text{Ba}_2\text{Si}_3\text{P}_6$  contains distorted  $\text{SiP}_4$  tetrahedra with angles ranging from 95.7–120° (Table S4), however stronger tetrahedral distortion was reported for another 1D compound in this system,  $\text{Ba}_4\text{Si}_3\text{P}_8$ .<sup>23</sup> The Si-P bonds in  $\text{Ba}_2\text{Si}_3\text{P}_6$  range from 2.210(2)–2.309(2) Å (Table S3), typical of Si-P bonds.<sup>22–24,26,28,40–42</sup>

Similarly, the P-P interatomic distance of 2.200(2) Å is typical for single covalent P-P bonds.<sup>23,43–46</sup> Assuming a coordination sphere of 3.5 Å, the Ba atoms are six or eight-coordinated with P, with Ba-P distances of 3.19–3.48 Å, which are in good agreement with other reported binary and ternary Ba phosphides.<sup>21,40,43,44</sup>

Several ternary silicon phosphides with different 1D polyanions have been reported, such as  $\text{K}_2\text{SiP}_2$ ,  $\text{Ca}_3\text{Si}_2\text{P}_4$ , and  $\text{Ba}_4\text{Si}_3\text{P}_8$ .<sup>22–24</sup> The chains of these compounds are shown in Figure 2, along with the chains in  $\text{Ba}_2\text{Si}_3\text{P}_6$ . The most simplistic chains are built from edge-shared  $\text{SiP}_4$  units, as seen in  $\text{K}_2\text{SiP}_2$  (Figure 2A).<sup>22</sup> Such 1D chains can increase in complexity if Si-Si bonds are introduced, as seen in  $\text{Ca}_3\text{Si}_2\text{P}_4$  (Figure 2B).<sup>24</sup> The zigzag chains in the structure of  $\text{Ca}_3\text{Si}_2\text{P}_4$  are formed by  $\text{Si}_2\text{P}_6$  units which are connected through sharing of two edges per  $\text{Si}_2\text{P}_6$  unit.<sup>24</sup> This type of bonding scheme is also common in binary 2D tetrel pnictides, like  $\text{SiP}$ .<sup>5–9</sup> The complexity of chains can be further increased through introduction of corner sharing and P-P covalent bonding, as in  $\text{Ba}_4\text{Si}_3\text{P}_8$  and title compound  $\text{Ba}_2\text{Si}_3\text{P}_6$ . (Figures 2C and 2D).<sup>23</sup>

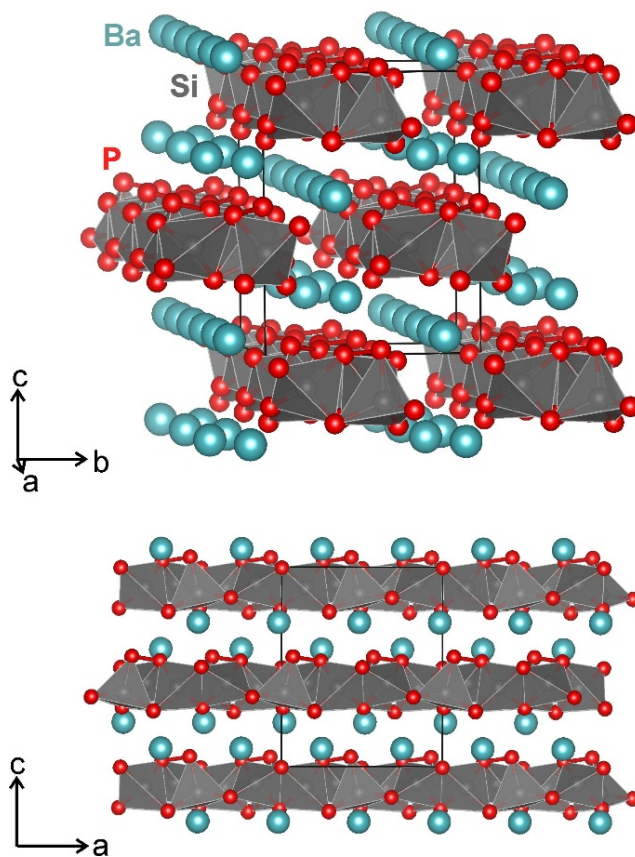


**Figure 1.** Crystal structure of  $\text{Ba}_2\text{Si}_3\text{P}_6$ : (top) a general view, (bottom) a projection down [010]. Ba: cyan; Si: grey; P: red;  $\text{SiP}_4$ : grey tetrahedra.

Although the chains of  $\text{Ba}_4\text{Si}_3\text{P}_8$  and  $\text{Ba}_2\text{Si}_3\text{P}_6$  are both formed through corner- and edge-sharing tetrahedra, as well as P-P bonding, the chains are drastically different. The connectivity in the chains of both structures can be described by three repeating tetrahedra (Figures 2C and 2D).

The Si-P chain in  $\text{Ba}_4\text{Si}_3\text{P}_8$  can be described as two tetrahedra (labeled 2 and 3 in Figure 2C) sharing an edge and connecting through a P-P bond. In addition, one of the edge sharing P also forms a P-P bridge to a tetrahedron 1, which is corner-shared with tetrahedron 2, and a tetrahedron 3 from a different 2-3 pair (Figure 2C). The remaining P corner of tetrahedron 1 is pointed towards Ba atoms.

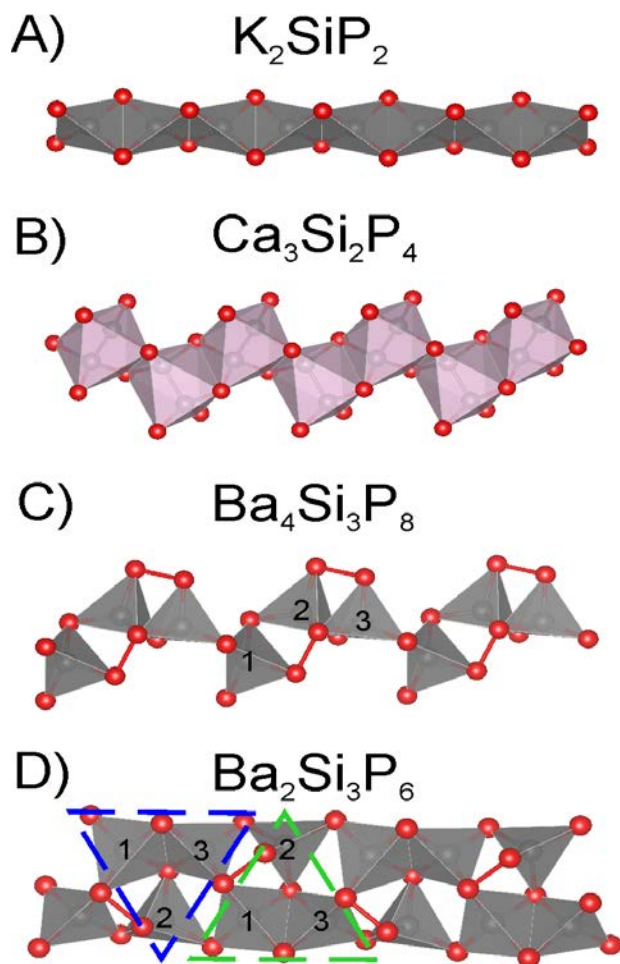


**Figure 2.** Bonding schemes found in 1D ternary silicon phosphide polyanionic chains: A) edge sharing, B) edge sharing and Si-Si bonding C) and D) edge sharing, corner sharing, and P-P bonding. For C) and D) individual tetrahedra and repeating units are highlighted. Cations are not shown for clarity.

Si-P chains in the  $\text{Ba}_2\text{Si}_3\text{P}_6$  structure can also be described as having two tetrahedra which share an edge (labeled 1 and 3 in Figure 2D). One of these shared P atoms is also shared as a corner with tetrahedron 2. The remaining four corners of tetrahedra 1 and 3 are all engaged in corner sharing with other tetrahedra. Covalent P-P bonds are formed through a shared corner of tetrahedra 1 and 3 which is linked to a corner of tetrahedron 2. The three tetrahedra of  $\text{Ba}_2\text{Si}_3\text{P}_6$  can be thought of as a single unit, which is repeated two different ways within the chain. This pattern is highlighted as blue and green triangles in Figure 2D. While the  $\text{Ba}_2\text{Si}_3\text{P}_6$  and  $\text{Ba}_4\text{Si}_3\text{P}_8$  structures contain the same types of  $\text{SiP}_4$  connectivity, one key difference is that all P atoms in  $\text{Ba}_2\text{Si}_3\text{P}_6$  are involved in inter-tetrahedra connectivity, while

in  $\text{Ba}_4\text{Si}_3\text{P}_8$  one P position is not involved, similarly to half of the P atoms in the chains of  $\text{K}_2\text{SiP}_2$  or a third of the P atoms in the chains of  $\text{Ca}_3\text{Si}_2\text{P}_4$ .<sup>22-24</sup>

$\text{Ba}_2\text{Si}_3\text{P}_6$  has the Wyckoff sequence  $a^{11}$ , space group  $Pna2_1$ , and Pearson symbol  $oP44$ . There are several different compounds with the same Wyckoff sequence, however none contain the complex chains found in  $\text{Ba}_2\text{Si}_3\text{P}_6$ , suggesting this to be a new structure type. Ternary compounds with the same Wyckoff sequence include  $\text{Sr}_2\text{P}_2\text{O}_7$  and  $\text{Eu}_2\text{Si}_2\text{O}_7$  which contain isolated  $\text{P}_2\text{O}_7$  and  $\text{Si}_2\text{O}_7$  units (corner sharing tetrahedra) respectively.<sup>47,48</sup> Another example is  $\text{Rb}_4\text{Al}_2\text{S}_5$  which is more structurally related. This phase contains  $\text{AlSi}_4$  tetrahedra which are connected through edge- and corner-sharing to form 1D chains, but no S-S covalent bonds.<sup>49</sup>

Due to similarity in scattering factor, initial Si and P positions were assigned based on the analysis of coordination number. In a subsequent refinement each position was assigned as P and as Si separately, and in both cases the occupancy was refined. It was determined that the initial assignment based on coordination number was correct, resulting in smaller than 4 e.s.d from 100% occupancy for the correct atom type, compared to the  $> 5$  e.s.d. for the opposite atom type. Furthermore, energy dispersive X-ray spectroscopy (EDS) on a cold pressed pellet of  $\text{Ba}_2\text{Si}_3\text{P}_6$  suggests a sample composition with a Ba:Si:P ratio of 2.4(1):3.0:5.8(1). EDS results are often skewed in compounds containing heavy and light elements. However, the ratio of light elements, Si:P = 1:1.9(1), agrees well with the single crystal refinement, Si:P = 1:2.

XPS analysis of a sintered pellet of  $\text{Ba}_2\text{Si}_3\text{P}_6$  sample shows that the  $\text{Ba}3d_{5/2}$  binding energy is 779.7 eV, which is consistent with ionic  $\text{Ba}^{2+}$  compounds such as  $\text{BaS}$  (Figure S6).<sup>50</sup> For Si, a broad asymmetric peak is observed, which can be deconvoluted into two components. The main contribution to the Si peak, with binding energy of 102.3 eV, is typical of silicates and is attributed to surface oxidation of the sample, while the lower binding energy (9% of Si peak) of 100.6 eV is characteristic of elemental silicon or covalently bonded Si, as in  $\text{SiC}$ , which is from the pristine sample.<sup>50,51</sup> The P spectrum clearly has two peaks with the higher binding energy of 132.9 eV typical for phosphates.<sup>50,52</sup> This is attributed to surface oxidation of the sample, while the lower binding energy at 130.1 eV is assumed to be from pristine sample as this is typical for covalently bonded P, as in  $\text{GaP}$  and  $\text{InP}$ .<sup>50</sup> The pristine P species corresponds to 45% of the overall intensity of P peak. The partial Si and P surface oxidation is confirmed by the presence and binding energy of the  $\text{O}1s$  peak.<sup>50</sup> Furthermore, comparing the intensities of pristine Si and P components, taking into account corresponding cross-sections, the Si:P ratio is 1:1.9, which is in good agreement with single crystal and EDS results for  $\text{Ba}_2\text{Si}_3\text{P}_6$ . Similar surface oxidation of air-stable phosphides  $\text{Si}_{130}\text{P}_{42}\text{Te}_{21.5}$  and  $\text{NiP}_2$  were reported.<sup>51,52</sup>

The complex chain structure of  $\text{Ba}_2\text{Si}_3\text{P}_6$  suggests that this material may exhibit low thermal conductivity due to alternating covalent and ionic bonding across the structure. Thermal transport properties of  $\text{Ba}_2\text{Si}_3\text{P}_6$  were measured using sintered 5 mm  $\varnothing$  pellet with 95% geometrical density.



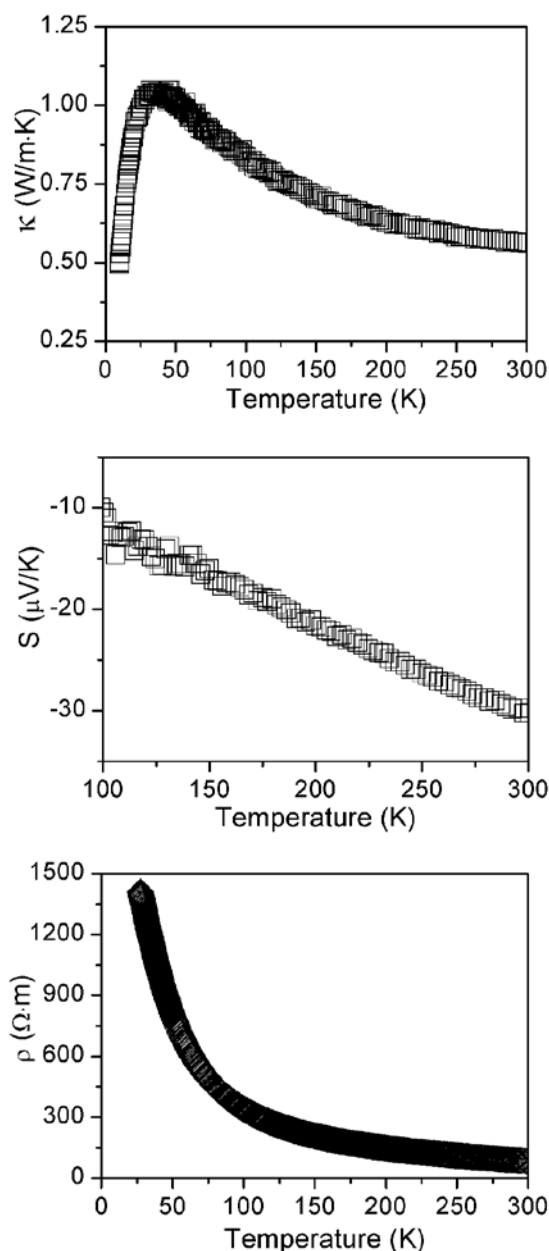


**Figure 3.** Thermal conductivity (top), thermopower (middle), and electrical resistivity (bottom) of  $\text{Ba}_2\text{Si}_3\text{P}_6$ . Thermopower is shown down to 100 K, below this temperature the measurements become unreliable due to too high resistivity.

$\text{Ba}_2\text{Si}_3\text{P}_6$  exhibits thermal conductivity temperature dependence which is typical for crystalline materials with a peak at 40 K and steady decrease at higher temperatures. The room temperature thermal conductivity is  $0.56 \text{ W m}^{-1} \text{ K}^{-1}$  at 300 K (Figure 3 top). Due to high resistivity, the electronic contribution to the thermal conductivity is negligible, below 0.01%, and the observed values correspond to predominantly lattice thermal conductivity. Such ultra-low thermal conductivity may stem from overall complexity of the crystal structure with alternating regions of covalent and ionic bonding as revealed by ELF and COHP analyses

(*vide infra*). Thermal conductivity of  $0.56 \text{ W m}^{-1} \text{ K}^{-1}$  at 300 K is comparable to that of state-of-the-art thermoelectric materials, such as  $\text{Yb}_{14}\text{MnSb}_{11}$  ( $0.7 \text{ W m}^{-1} \text{ K}^{-1}$  at 300 K),  $\text{Bi}_{0.5}\text{Sb}_{1.5}\text{Te}_3$  ( $\sim 0.7 \text{ W m}^{-1} \text{ K}^{-1}$  at 300 K), [010] direction of the  $\text{SnSe}$  single crystal ( $0.7 \text{ W m}^{-1} \text{ K}^{-1}$  at 300 K),  $\text{Zn}_8\text{Sb}_7$  ( $0.6 \text{ W m}^{-1} \text{ K}^{-1}$  at 400 K),  $\text{Ba}_8\text{Cu}_{14}\text{Ge}_6\text{P}_{26}$  ( $0.77 \text{ W m}^{-1} \text{ K}^{-1}$  at 300 K), and  $\text{La}_x\text{Ba}_{8-x}\text{Cu}_{16}\text{P}_{30}$  ( $\sim 1.1 \text{ W m}^{-1} \text{ K}^{-1}$  at 400 K).<sup>53-58</sup>  $\text{Ba}_2\text{Si}_3\text{P}_6$  displays a relatively low absolute value of Seebeck coefficient ( $-30 \text{ } \mu\text{V/K}$  at 300 K) and high resistivity ( $83 \text{ } \Omega\text{m}$  at 300 K) (Figure 3 middle and bottom). The negative nature of the Seebeck and temperature dependence of resistivity suggest  $\text{Ba}_2\text{Si}_3\text{P}_6$  to be a *n*-type semiconductor. The overall thermoelectric figure of merit,  $zT$ , for  $\text{Ba}_2\text{Si}_3\text{P}_6$  is 0.006 at 300 K (Figure S5). To improve the resistivity and thermopower to useful thermoelectric application levels, the doping of  $\text{Ba}_2\text{Si}_3\text{P}_6$  is required to adjust the carrier concentration and mobility.<sup>59</sup>

The thermal stability of  $\text{Ba}_2\text{Si}_3\text{P}_6$  was investigated using differential scanning calorimetry (DSC) (Figure S4) which shows that upon heating  $\text{Ba}_2\text{Si}_3\text{P}_6$  melts at  $1318(3) \text{ K}$ . Upon cooling there is an intense recrystallization peak with an onset of  $1284 \text{ K}$ . After DSC measurements, PXRD confirmed that the recrystallized phase was indeed  $\text{Ba}_2\text{Si}_3\text{P}_6$ . This holds certain promise that large single crystals of the title compound may be grown using the Bridgman technique, although substantial experimental efforts are required to verify this claim. The Bridgman method is suitable to grow cm-sized single crystals of phosphides with high P content.<sup>57,60</sup>

Considering the electron balance from the point of view of covalent Si-P and P-P bonding, tetra-coordinated Si atoms in the polyanionic chain have 0 formal oxidation state as well as three-coordinated phosphorus atoms. Two coordinated phosphorus atoms have -1 formal oxidation state, leading to the electron balanced composition,  $(\text{Ba}^{2+})_2(\text{Si}^0)_3(\text{P}^0)_2(\text{P}^{1-})_4$ . Alternatively, a polar scheme can be considered where Si is treated as  $\text{Si}^{4+}$  and all electrons are transferred to the phosphorus polyanion. In such a case, P bonded only to Si atoms have formal oxidation states of -3, while P connected to one P atom has a formal oxidation state of -2. This consideration also leads to an electron-balanced composition,  $(\text{Ba}^{2+})_2(\text{Si}^{4+})_3(\text{P}^{2-})_2(\text{P}^{3-})_4$ . Electron localization function bonding analysis indicates that the first scenario with covalent Si-P interactions is correct (Figure 4) in agreement with experimental XPS results. Every Si atom forms four covalent bonds to P atoms (Figure 4B), while P atoms in addition to forming covalent Si-P and P-P bonds complete their octet tetrahedral coordination with electron lone pairs. In accordance with Zintl-Klemm electron count, three-bonded (*3b*) P atoms have one electron-lone pair, while two-bonded (*2b*) P atoms have two electron lone pairs (Figure 4A). ELF distribution around the Ba cations is almost spherical which is typical for non-directed electrostatic interactions between  $\text{Ba}^{2+}$  and anions.<sup>44,61,62</sup> To evaluate the relative strength of the interactions crystal orbital Hamilton population (COHP) analysis was applied (Figure S7). COHP plots show that Si-P is predominantly optimized with all of bonding states occupied and the majority of anti-bonding states remain empty (Figures S7b-d). The P-P

bonding is not completely optimized and substantial anti-bonding states at  $-0.5$  eV are occupied (Figure S7a). The ICOHP values range from 2.98 eV/bond to 3.89 eV/bond for Si-P covalent interactions and 3.78 eV/bond for the P-P covalent bonds. The shortest electrostatic Ba-P interactions of 3.19 Å are significantly weaker, 0.82 eV/bond. The performed bonding analysis confirms the proposed anisotropic chemical bonding in  $\text{Ba}_2\text{Si}_3\text{P}_6$ . Along the chain propagation direction, [100], there is strong covalent bonding in the Si-P chains, while in the direction perpendicular to the chains, alternating stronger Si-P covalent and weaker Ba-P electrostatic interactions occur.

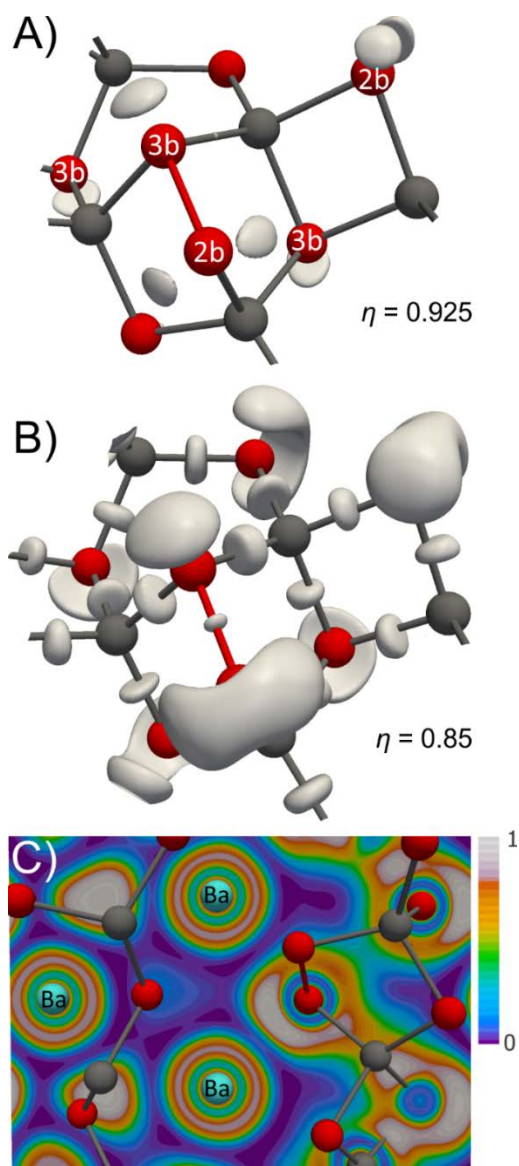


**Figure 4.** Electron localization function (ELF,  $\eta$ ) analysis of chemical bonding in  $\text{Ba}_2\text{Si}_3\text{P}_6$ : A) and B) 3D isosurfaces of ELF with  $\eta = 0.925$  and  $\eta = 0.85$ ; C) Coloring of the ELF distributions for a slice of the crystal structure containing Ba atoms. Ba: cyan; Si: grey; P: red.

The electronic structure of  $\text{Ba}_2\text{Si}_3\text{P}_6$  calculated using the TB-LMTO-ASA is shown in Figure 5. The conduction band is formed through near equal contribution from Ba, Si, and P, while the P 3p orbitals contributions dominate in the valence band. The partial density of states suggests that there is strong covalent bonding in the  $\text{SiP}_4$  chains because of the good mixing of Si and P orbitals, agreeing with the ELF results. This result was also confirmed with a second calculation method, VASP (Figure S8), which is in good agreement with the DOS calculated using LMTO. Further analysis of the DOS indicates band gaps of 1.57 eV (LMTO) and 1.42 eV (VASP). Considering that both methods generally underestimate bandgaps, these calculations are in good agreement with the observed dark red color of  $\text{Ba}_2\text{Si}_3\text{P}_6$ . The LMTO band structure indicates that  $\text{Ba}_2\text{Si}_3\text{P}_6$  is a pseudo-direct semiconductor because the direct bandgap at the  $\Gamma$  point is only 0.02 eV larger than the indirect one. Transport property measurements indicated *n*-type semiconducting properties which is presumably due to the defect chemistry such as P-vacancies.

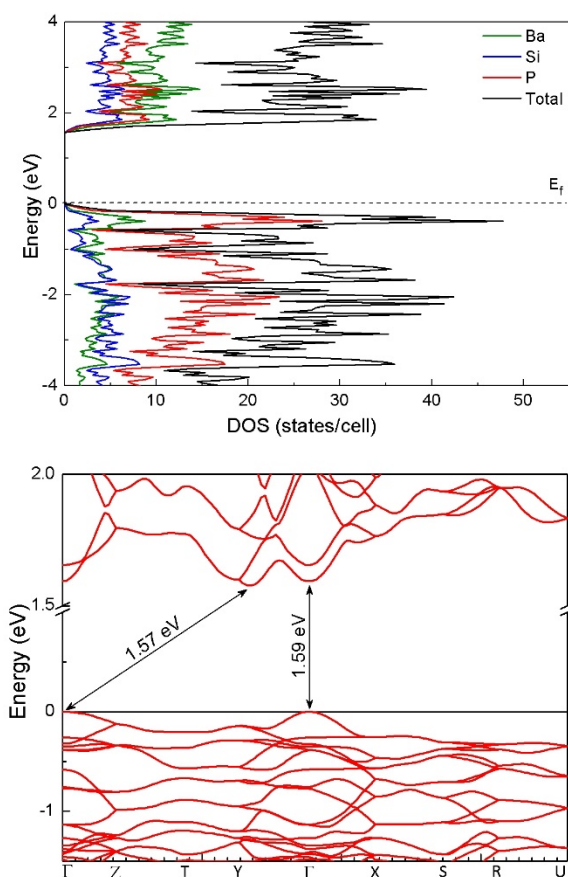


**Figure 5.** Density of states (top) and band structure (bottom) of  $\text{Ba}_2\text{Si}_3\text{P}_6$  (TB-LMTO-ASA). The Fermi level ( $E_f$ ) is set to 0 eV.

To confirm the calculated band gap, solid state UV/Vis diffuse reflectance was performed (Figure S9). Tauc plot analysis of the UV/Vis data, shown in Figure 6, indicates  $\text{Ba}_2\text{Si}_3\text{P}_6$  has a direct band gap of 1.88(1) eV. This experimental result is in good agreement with our calculations and the red color of the compound. Due to the suitable band gap and non-

centrosymmetric nature of  $\text{Ba}_2\text{Si}_3\text{P}_6$ , this material could have potential nonlinear optical (NLO) applications for second harmonic generation.

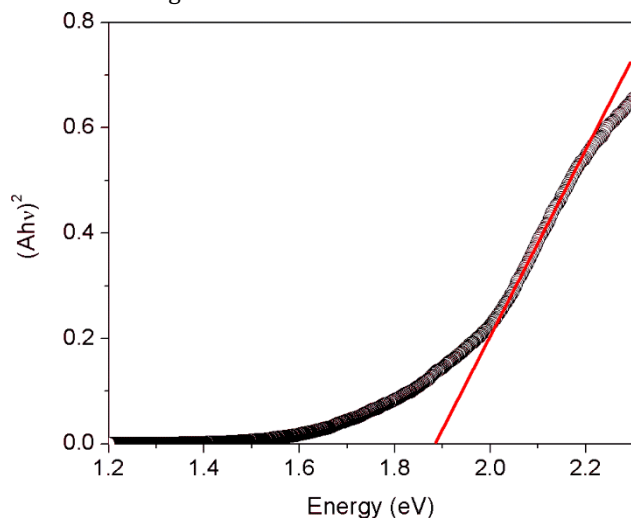


**Figure 6.** Direct band gap Tauc plot for solid state UV/Vis spectrum of  $\text{Ba}_2\text{Si}_3\text{P}_6$ .

Second harmonic generation (SHG) measurements were performed by means of the Kurtz and Perry method.<sup>63</sup>  $\text{Ba}_2\text{Si}_3\text{P}_6$  exhibits a good powder SHG response that is comparable to that of benchmark  $\text{AgGaS}_2$  at particle sizes of 55–88  $\mu\text{m}$  utilizing a 2.09  $\mu\text{m}$  laser source (Figure 7).  $\text{Ba}_2\text{Si}_3\text{P}_6$  shows better SHG performance ( $0.9 \times \text{AgGaS}_2$ ) than recently discovered  $\text{MgSiAs}_2$  ( $0.6 \times \text{AgGaS}_2$ ).<sup>27</sup> Due to the narrow optical bandgap (both from theory calculation and optical measurements) and long shortwave absorption edge (up to 1  $\mu\text{m}$ ),  $\text{Ba}_2\text{Si}_3\text{P}_6$  is expected to perform better in SHG under longer wavelength lasers, such as a carbon dioxide laser. For example, a similar situation for  $\text{CdGeAs}_2$  was also observed, which exhibits large NLO efficiency (236 pm/V) at a longer excitation wavelength.<sup>64</sup> Thus,  $\text{Ba}_2\text{Si}_3\text{P}_6$  can also be considered a promising IR-NLO material with a suitable excitation source.

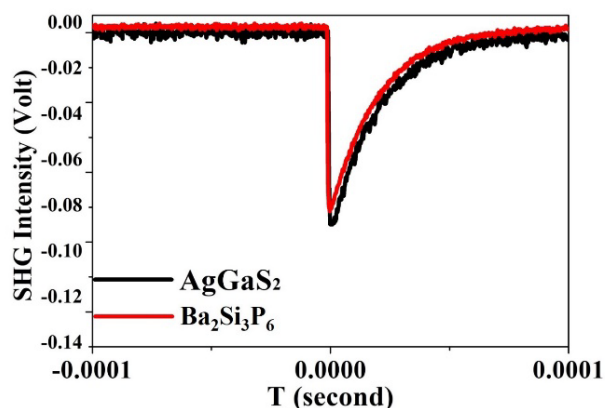


**Figure 7.** Comparison of SHG intensity of  $\text{Ba}_2\text{Si}_3\text{P}_6$  and  $\text{AgGaS}_2$  at 55–88  $\mu\text{m}$  particle size.

The laser damage threshold (LDT) of  $\text{Ba}_2\text{Si}_3\text{P}_6$  was also measured by adjusting the laser output energy and observing the color change using an optical microscope. Results

show that  $\text{Ba}_2\text{Si}_3\text{P}_6$  exhibits a much higher LDT (48.5  $\text{MW}/\text{cm}^2$ ) than that of  $\text{AgGaS}_2$  (29.6  $\text{MW}/\text{cm}^2$ ) (Table 1), which is also higher than that of recently discovered  $\text{MgSiAs}_2$  (33.2  $\text{MW}/\text{cm}^2$ ) as well as those of other typical IR-NLO materials such as  $\text{AgGaSe}_2$  and  $\text{ZnGeP}_2$ .<sup>27,38,39,64,65</sup> Recently reported  $\text{MnSiP}_2$  NLO material crystallizing in the chalcopyrite structure type also exhibits high LDT, although measured on a single crystal (70  $\text{MW}/\text{cm}^2$ ), thus confirming that silicon-phosphides are a good platform for novel NLO materials.<sup>60</sup> The promising SHG coefficient in addition to the high LDT make  $\text{Ba}_2\text{Si}_3\text{P}_6$  a promising candidate for IR-NLO applications. The growth of large high-quality single crystals of  $\text{Ba}_2\text{Si}_3\text{P}_6$  is underway.

**Table 1.** LDTs of  $\text{Ba}_2\text{Si}_3\text{P}_6$  and reference  $\text{AgGaS}_2$ .

Compound	Damage Energy (mJ)	Spot Diameter (mm)	LDT ( $\text{MW}/\text{cm}^2$ )
$\text{AgGaS}_2$	0.58	0.5	29.6
$\text{Ba}_2\text{Si}_3\text{P}_6$	0.94	0.5	48.5

## Conclusion

Novel non-centrosymmetric alkaline-earth tetrel-pnictide,  $\text{Ba}_2\text{Si}_3\text{P}_6$  was discovered, synthesized, and characterized. The unique crystal structure of this compound is built of 1D Si-P chains in which  $\text{SiP}_4$  tetrahedra are connected through corner sharing, edge sharing, as well as P-P bonding. The chains are separated by  $\text{Ba}^{2+}$  cations. This complex 1D chain structure with alternating covalent and ionic bonding demonstrates ultra-low thermal conductivity of  $0.56 \text{ W m}^{-1} \text{ K}^{-1}$  at 300 K, comparable to the thermal conductivity of the state-of-the-art thermoelectric materials.  $\text{Ba}_2\text{Si}_3\text{P}_6$  exhibits promising SHG and LDT results, outperforming the current standard in IR-NLO materials,  $\text{AgGaS}_2$ . These promising results stem from the strong covalent Si-P and P-P bonding in the 1D chains. This work further expands the knowledge of non-centrosymmetric tetrel-pnictide compounds with possible nonlinear optic applications.

## ASSOCIATED CONTENT

**Supporting Information.** Experimental details, figures, and tables pertinent to characterization techniques used: powder and single crystal X-ray diffraction, energy dispersive X-ray spectroscopy, differential scanning calorimetry, spark plasma sintering, transport property measurements, X-ray photoelectron spectroscopy, electronic structure calculations, electron localization function, UV/Vis spectroscopy, and powder second harmonic generation. This material is available free of charge via the Internet at <http://pubs.acs.org>.

## AUTHOR INFORMATION

Corresponding Author

Dr. Kirill Kovnir, [kovnir@iastate.edu](mailto:kovnir@iastate.edu)

## Author Contributions

The manuscript was written through contributions of all authors.

## Funding Sources



This work was supported by the Laboratory Research and Development Program of the Ames Laboratory under the U.S. Department of Energy Contract No. DE-AC02-07CH11358. We thank the National Science Foundation MRI program, Grant 1531193, for the funding for the Bruker D8 Venture single-crystal X-ray diffractometer.

## ACKNOWLEDGMENT

We thank Prof. J. Vela for access to the UV/Vis spectrometer, Prof. J. V. Zaikina for access to the SPS, and Dr. D. Jing for help with the XPS measurements.

## REFERENCES

- (1) Lee, K.; Kaseman, D.; Sen, S.; Hung, I.; Gan, Z.; Gerke, B.; Pöttgen, R.; Feygenson, M.; Neufeld, J.; Lebedev, O.I.; Kovnir, K. Intricate short-range ordering and strongly anisotropic transport properties of  $\text{Li}_{1-x}\text{Sn}_{2+x}\text{As}_2$ . *J. Amer. Chem. Soc.* **2015**, *137*, 3622-3630.
- (2) Goto, Y.; Miura, A.; Moriyoshi, C.; Kuroiwa, Y.; Matsuda, T. D.; Aoki, Y.; Mizuguchi, Y.,  $\text{Na}_{1-x}\text{Sn}_2\text{P}_2$  as a new member of van der Waals-type layered tin pnictide superconductors. *Sci. Rep.* **2018**, *8*, 12852.
- (3) Goto, Y.; Yamada, A.; Matsuda, T. D.; Aoki, Y.; Mizuguchi, Y., SnAs-Based Layered Superconductor  $\text{NaSn}_2\text{As}_2$ . *J. Phys. Soc. Jpn.* **2017**, *86*, 123701.
- (4) Pomerantseva, E.; Resini, C.; Kovnir, K.; Kolen'ko, Yu. V. Emerging nanostructured electrode materials for water electrolysis and rechargeable beyond Li-ion batteries. *Adv. Phys. X*, **2017**, *2*, 211-253.
- (5) Wadsten, T., The Crystal Structure of SiAs. *Acta Chem. Scand.* **1965**, *19*, 1232-1238.
- (6) Wadsten, T., The Crystal Structures of  $\text{SiP}_2$ ,  $\text{SiAs}_2$ , GeP. *Acta Chem. Scand.* **1967**, *21*, 593-594.
- (7) Wadsten, T., Preparative and crystal structure studies on orthorhombic silicon monophosphide. *Chem. Scripta*, **1975**, *8*, 63-69.
- (8) Stohr, H.; Klemm, W., Über Zweistoffsysteme mit Germanium. II) Germanium/Arsen, Germanium/Antimon, Germanium/Wismut. *Z. Anorg. Allg. Chem.* **1940**, *244*, 205-223.
- (9) Klemm, W.; Pirscher, P., Über Siliciumarsenide. *Z. Anorg. Allg. Chem.* **1941**, *247*, 211-220.
- (10) Bryden, J. H., The Crystal Structures of the Germanium-Arsenic Compounds. I. Germanium Diarsenide,  $\text{GeAs}_2$ . *Acta Crystallogr.* **1962**, *15*, 167-171.
- (11) Lee, K.; Kamali, S.; Ericsson, T.; Bellard, M.; Kovnir, K., GeAs: Highly anisotropic van der Waals thermoelectric material. *Chem. Mater.* **2016**, *28*, 2776-2785.
- (12) Lee, K.; Synnestevedt, S.; Bellard, M.; Kovnir, K., GeP and  $(\text{Ge}_{1-x}\text{Sn}_x)(\text{P}_{1-y}\text{Ge}_y)$  ( $x \approx 0.12$ ,  $y \approx 0.05$ ): Synthesis, structure, and properties of two-dimensional layered tetrel phosphides. *J. Solid State Chem.* **2015**, *224*, 62-70.
- (13) Mark, J.; Hanrahan, M. P.; Woo, K. E.; Lee, S.; Rossini, A. J.; Kovnir, K., Chemical and Electrochemical Lithiation of van der Waals Tetrel-Arsenides. *Chem. Eur. J.* **2019**, *25*, 6392-6401.
- (14) Cheng, A. Q.; He, Z.; Zhao, J.; Zeng, H.; Chen, R. S., Monolayered Silicon and Germanium Monopnictide Semiconductors: Excellent Stability, High Absorbance, and Strain Engineering of Electronic Properties. *ACS Appl. Mater. Interfaces* **2018**, *10*, 5133-5139.
- (15) Guo, J.; Liu, Y.; Ma, Y.; Zhu, E.; Lee, S.; Lu, Z.; Zhao, Z.; Xu, C.; Lee, S. J.; Wu, H.; Kovnir, K.; Huang, Y.; Duan, X., Few-Layer GeAs Field-Effect Transistors and Infrared Photodetectors. *Adv. Mater.* **2018**, *30*, e1705934.
- (16) Zhou, Z.; Long, M.; Pan, L.; Wang, X.; Zhong, M.; Blei, M.; Wang, J.; Fang, J.; Tongay, S.; Hu, W.; Li, J.; Wei, Z., Perpendicular Optical Reversal of the Linear Dichroism and Polarized Photodetection in 2D GeAs. *ACS Nano* **2018**, *12*, 12416-12423.
- (17) Yang, S.; Yang, Y.; Wu, M.; Hu, C.; Shen, W.; Gong, Y.; Huang, L.; Jiang, C.; Zhang, Y.; Ajayan, P. M., Highly In-Plane Optical and Electrical Anisotropy of 2D Germanium Arsenide. *Adv. Funct. Mater.* **2018**, *28*, 1707379.
- (18) Li, C.; Wang, S.; Zhang, X.; Jia, N.; Yu, T.; Zhu, M.; Liu, D.; Tao, X., Controllable seeded flux growth and optoelectronic properties of bulk o-SiP crystals. *CrystEngComm* **2017**, *19*, 6986-6991.
- (19) Li, C.; Wang, S.; Li, C.; Yu, T.; Jia, N.; Qiao, J.; Zhu, M.; Liu, D.; Tao, X., Highly sensitive detection of polarized light using a new group IV-V 2D orthorhombic SiP. *J. Mater. Chem. C* **2018**, *6*, 7219-7225.
- (20) Li, L.; Gong, P.; Sheng, D.; Wang, S.; Wang, W.; Zhu, X.; Shi, X.; Wang, F.; Han, W.; Yang, S.; Liu, K.; Li, H.; Zhai, T., Highly In-Plane Anisotropic 2D GeAs<sub>2</sub> for Polarization-Sensitive Photodetection. *Adv. Mater.* **2018**, *30*, e1804541.
- (21) Eisenmann, B.; Jordan, H.; Schafer, H., Zintl-Phasen mit Komplexen Anionen Darstellung und Struktur der o-Phosphosilikate und -Germanate  $\text{E}_4^{\text{II}}\text{E}_4^{\text{IV}}\text{P}_4$  (mit  $\text{E}^{\text{II}} = \text{Ca, Sr, Ba}$  und  $\text{E}^{\text{IV}} = \text{Si, Ge}$ ) *Mat. Res. Bull.* **1982**, *17*, 95-99.
- (22) Eisenmann, B.; Somer, M.,  $\text{K}_2\text{SiP}_2$ , ein Phosphidopolysilikat(IV). *Z. Naturforsch.* **1984**, *39b*, 736-738.
- (23) Mark, J.; Dolyniuk, J.-A.; Tran, N.; Kovnir, K., Crystal and Electronic Structure and Optical Properties of  $\text{AE}_2\text{SiP}_4$  ( $\text{AE} = \text{Sr, Eu, Ba}$ ) and  $\text{Ba}_4\text{Si}_3\text{P}_8$ . *Z. Anorg. Allg. Chem.* **2019**, *645*, 242-247.
- (24) Zhang, X.; Yu, T.; Li, C.; Wang, S.; Tao, X., Synthesis and Crystal Structures of the Calcium Silicon Phosphides  $\text{Ca}_2\text{Si}_2\text{P}_4$ ,  $\text{Ca}_3\text{Si}_8\text{P}_{14}$  and  $\text{Ca}_3\text{Si}_2\text{P}_4$ . *Z. Anorg. Allg. Chem.* **2015**, *641*, 1545-1549.
- (25) Khatun, M.; Mar, A.,  $\text{NaGeAs}$ : Insertion of sodium into the layered semiconductor germanium arsenide GeAs. *Z. Naturforsch., B: J. Chem. Sci.* **2016**, *71*, 375-380.
- (26) Eisenmann, B.; Jordan, H.; Schafer, H.,  $\text{Ba}_3\text{Si}_4\text{P}_6$ , eine neue Zintlphase mit vernetzten  $\text{Si}_4\text{P}_5$ -Käfigen. *Z. Naturforsch.* **1984**, *39b*, 864-867.
- (27) Woo, K. E.; Wang, J.; Wu, K.; Lee, K.; Dolyniuk, J.-A.; Pan, S.; Kovnir, K., Mg-Si-As: An Unexplored System with Promising Nonlinear Optical Properties. *Adv. Funct. Mater.* **2018**, *28*, 1801589.
- (28) Toffoletti, L.; Kirchhain, H.; Landesfeind, J.; Klein, W.; van Wullen, L.; Gasteiger, H. A.; Fassler, T. F., Lithium Ion Mobility in Lithium Phosphidosilicates: Crystal Structure,  $^7\text{Li}$ ,  $^{29}\text{Si}$ , and  $^{31}\text{P}$  MAS NMR Spectroscopy, and Impedance Spectroscopy of  $\text{Li}_8\text{SiP}_4$  and  $\text{Li}_2\text{SiP}_2$ . *Chem. Eur. J.* **2016**, *22*, 17635-17645.
- (29) Ohmer, M. C.; Pandey, R., Emergence of Chalcopyrites as Nonlinear Optical Materials. *Mat. Res. Bull.* **1998**, *23*, 16-22.
- (30) Chung, I.; Kanatzidis, M. G., Metal Chalcogenides: A Rich Source of Nonlinear Optical Materials. *Chem. Mater.* **2013**, *26*, 849-869.
- (31) Jackson, A. G.; Ohmer, M. C.; LeClair, S. R., Relationship of the second order nonlinear optical coefficient to energy gap in inorganic non-centrosymmetric crystals. *Infrared Phys. Technol.* **1997**, *38*, 233-244.
- (32) Li, M. Y.; Li, B. X.; Lin, H.; Shi, Y. F.; Ma, Z.; Wu, L. M.; Wu, X. T.; Zhu, Q. L., Ternary Mixed-Metal  $\text{Cd}_4\text{GeSe}_6$ : Remarkable Nonlinear-

Optical Properties Based on a Tetrahedral-Stacking Framework. *Inorg. Chem.* **2018**, *57*, 8730-8734.

(33) Yin, W.; Iyer, A. K.; Li, C.; Yao, J.; Mar, A., Ba<sub>5</sub>CdGa<sub>6</sub>Se<sub>15</sub>, a congruently-melting infrared nonlinear optical material with strong SHG response. *J. Mater. Chem. C* **2017**, *5*, 1057-1063.

(34) Dou, Y.; Chen, Y.; Li, Z.; Iyer, A. K.; Kang, B.; Yin, W.; Yao, J.; Mar, A., SrCdGeS<sub>4</sub> and SrCdGeSe<sub>4</sub>: Promising Infrared Nonlinear Optical Materials with Congruent-Melting Behavior. *Cryst. Growth Des.* **2019**, *19*, 1206-1214.

(35) Brant, J.A.; Clark, D.J.; Kim, Y.S.; Jang, J.I.; Weiland, A.; Aitken, J.A., Outstanding Laser Damage Threshold in Li<sub>2</sub>MnGeS<sub>4</sub> and Tunable Optical Nonlinearity in Diamond-Like Semiconductors. *Inorg. Chem.* **2015**, *54*, 2809-2819.

(36) Lin, H.; Chen, L.; Zhou, L. J.; Wu, L. M., Functionalization based on the substitutional flexibility: strong middle IR nonlinear optical selenides AX<sup>II</sup><sub>4</sub>X<sup>III</sup><sub>5</sub>Se<sub>12</sub>. *J. Am. Chem. Soc.* **2013**, *135*, 12914-21.

(37) Wu, K.; Yang, Z.; Pan, S., Na<sub>2</sub>Hg<sub>3</sub>M<sub>2</sub>S<sub>8</sub> (M = Si, Ge, and Sn): New Infrared Nonlinear Optical Materials with Strong Second Harmonic Generation Effects and High Laser-Damage Thresholds. *Chem. Mater.* **2016**, *28*, 2795-2801.

(38) Luo, X.; Li, Z.; Guo, Y.; Yao, J.; Wu, Y. Recent progress on new infrared nonlinear optical materials with application prospect. *J. Solid State Chem.* **2019**, *270*, 674-687.

(39) Chu, Y.; Li, G.; Su, X.; Wu, K.; Pan, S. A review on the development of infrared nonlinear optical materials with triangular anionic groups. *J. Solid State Chem.* **2019**, *271*, 266-272.

(40) Haffner, A.; Johrendt, D. Synthesis, Crystal Structure, and Chemical Bonding of Ba<sub>2</sub>SiP<sub>4</sub>. *Z. Anorg. Allg. Chem.* **2017**, *643*, 1717-1720.

(41) Kaiser, P.; Jeitschko, W., The Rare Earth Silicon Phosphides LnSi<sub>2</sub>P<sub>6</sub> (Ln = La, Ce, Pr, and Nd). *J. Solid State Chem.* **1996**, *124*, 346-352.

(42) Vincent, H.; Kreisel, J.; Perrier, C.; Chaix-Pluchery, O.; Chaudouet, P.; Madar, R.; Genet, F.; Lucazeau, G., Synthesis, Crystal Structure, Raman Spectroscopy, and Physical Characterization of a New Cobalt Phospho-Silicide CoSi<sub>3</sub>P<sub>3</sub>. *J. Solid State Chem.* **1996**, *124*, 366-373.

(43) Dolyniuk, J. A.; He, H.; Ivanov, A. S.; Boldyrev, A. I.; Bobev, S.; Kovnir, K., Ba and Sr Binary Phosphides: Synthesis, Crystal Structures, and Bonding Analysis. *Inorg. Chem.* **2015**, *54*, 8608-16.

(44) Dolyniuk, J. A.; Kaseman, D. C.; Sen, S.; Zhao, J.; Osterloh, F. E.; Kovnir, K., mP-BaP<sub>3</sub>: a new phase from an old binary system. *Chem. Eur. J.* **2014**, *20*, 10829-37.

(45) von Schnering, H. G.; Menge, G., Das Magnesiumpolyphosphid MgP<sub>4</sub>. *Z. Anorg. Allg. Chem.* **1976**, *422*, 219-225.

(46) von Schnering, H. G.; Wittmann, M., Europium (II) Heptaphosphide EuP<sub>7</sub> [1]. *Z. Naturforsch., B: Anorg. Chem., Org. Chem.* **1980**, *35B*, 824-831.

(47) Grenier, J.-C.; Masse, R., Mise au point sur la structure cristallographique de α-Sr<sub>2</sub>P<sub>2</sub>O<sub>7</sub>. *Bull. Soc. Fr. Mineral. Cristallogr.* **1969**, *92*, 91-92.

(48) Felsche, J. *The crystal chemistry of the rare-earth silicates*. In: Rare Earths. Structure and bonding, Springer, Berlin, Heidelberg **1973**; *13*, pp 99-197.

(49) Winkler, V.; Schlosser, M.; Pfitzner, A., Synthesis and Crystal Structures of Rb<sub>4</sub>Al<sub>2</sub>S<sub>5</sub> and Cs<sub>4</sub>In<sub>2</sub>S<sub>5</sub>. *Z. Anorg. Allg. Chem.* **2015**, *641*, 549-556.

(50) Moulder, J. F.; Stickle, W. F.; Sobol, P. E.; Bomben, K. D., *Handbook of X-ray Photoelectron Spectroscopy*. Physical Electronics, Inc.: Eden Prairie, Minnesota, 1995.

(51) Zaikina, J. V.; Mori, T.; Kovnir, K.; Teschner, D.; Senyshyn, A.; Schwarz, U.; Grin, Y.; Shevelkov, A. V., Bulk and surface structure and high-temperature thermoelectric properties of inverse clathrate-III in the Si-P-Te system. *Chem. Eur. J.* **2010**, *16*, 12582-9.

(52) Owens-Baird, B.; Xu, J.; Petrovykh, D. Y.; Bondarchuk, O.; Ziouani, Y.; González-Ballesteros, N.; Yox, P.; Sapountzi, F. M.; Niemantsverdriet, H.; Kolen'ko, Y. V.; Kovnir, K., NiP<sub>2</sub>: A Story of Two Divergent Polymorphic Multifunctional Materials. *Chem. Mater.* **2019**, *31*, 3407-3418.

(53) Hu, Y.; Cerretti, G.; Wille, E.L.K.; Bux, S.K.; Kauzlarich, S.M. The remarkable crystal chemistry of the Ca<sub>14</sub>AlSb<sub>11</sub> structure type, magnetic and thermoelectric properties. *J. Solid State Chem.* **2019**, *271*, 88-102.

(54) Qin, H.; Liu, Y.; Zhang, Z.; Wang, Y.; Cao, J.; Cai, W.; Zhang, Q.; Sui, J., Improved thermoelectric performance of p-type Bi<sub>0.5</sub>Sb<sub>1.5</sub>Te<sub>3</sub> through Mn doping at elevated temperature. *Mater. Today Phys.* **2018**, *6*, 31-37.

(55) Zhao, L. D.; Lo, S. H.; Zhang, Y.; Sun, H.; Tan, G.; Uher, C.; Wolverton, C.; Dravid, V. P.; Kanatzidis, M. G., Ultralow thermal conductivity and high thermoelectric figure of merit in SnSe crystals. *Nature* **2014**, *508*, 373-7.

(56) Wang, J.; Kovnir, K., Elusive beta-Zn<sub>8</sub>Sb<sub>7</sub>: A New Zinc Antimonide Thermoelectric. *J. Am. Chem. Soc.* **2015**, *137*, 12474-7.

(57) Wang, J.; Lebedev, O. I.; Lee, K.; Dolyniuk, J. A.; Klavins, P.; Bux, S.; Kovnir, K., High-efficiency thermoelectric Ba<sub>8</sub>Cu<sub>14</sub>Ge<sub>6</sub>P<sub>26</sub>: bridging the gap between tetrel-based and tetrel-free clathrates. *Chem. Sci.* **2017**, *8*, 8030-8038.

(58) Wang, J.; He, Y.; Mordvinova, N.E.; Lebedev, O.I.; Kovnir, K. The smaller the better: Hosting trivalent rare-earth guests in Cu-P clathrate cages. *Chem.* **2018**, *4*, 1465-1475.

(59) Owens-Baird, B.; Heinrich, S.; Kovnir, K. Thermoelectric Materials. *Encyclop. Inorg. Bioinorg. Chem.* **2017**, 1-35.

(60) Yu, T.; Wang, S.; Zhang, X.; Li, C.; Qiao, J.; Jia, N.; Han, B.; Xia, S.-Q.; Tao, X. MnSiP<sub>2</sub>: A New Mid-IR Ternary Phosphide with Strong SHG Effect and Ultrabroad Transparency Range. *Chem. Mater.* **2019**, *31*, 2010-2018.

(61) Dolyniuk, J.-A.; Wang, J.; Lee, K.; Kovnir, K., Twisted Kelvin Cells and Truncated Octahedral Cages in the Crystal Structures of Unconventional Clathrates, AM<sub>2</sub>P<sub>4</sub> (A = Sr, Ba; M = Cu, Ni). *Chem. Mater.* **2015**, *27*, 4476-4484.

(62) Fulmer, J.; Kaseman, D. C.; Dolyniuk, J. A.; Lee, K.; Sen, S.; Kovnir, K., BaAu<sub>2</sub>P<sub>4</sub>: layered zintl polyphosphide with infinite <sup>1</sup>/<sub>∞</sub>(P<sup>-</sup>) chains. *Inorg. Chem.* **2013**, *52*, 7061-7.

(63) Kurtz, S. K.; Perry, T. T., A Powder Technique for the Evaluation of Nonlinear Optical Materials. *J. Appl. Phys.* **1968**, *39*, 3798-3813.

(64) Byer, R. L.; Kildal, H.; Feigelson, R. S., CdGeAs<sub>2</sub> - A New Nonlinear Crystal Phasematchable at 10.6 μm. *Appl. Phys. Lett.* **1971**, *19*, 237-240.

(65) Zhu, T.; Chen, X.; Qin, J., Research progress on mid-IR nonlinear optical crystals with high laser damage threshold in China. *Front. Chem. China*, **2011**, *6*, 1-8.



